Contents lists available at ScienceDirect

Engineering Structures

Unsupervised autoencoders with features in the electromechanical impedance domain for early damage assessment in FRP-strengthened concrete elements

Ricardo Perera [a,*], Javier Montes [a], Alejandra Gómez [a], Cristina Barris [b], Marta Baena [b]

[a] Department of Mechanical Engineering, Universidad Politécnica de Madrid, 28006 Madrid, Spain
[b] Analysis and Advanced Materials for Structural Design (AMADE), Polytechnic School, University of Girona, 17003 Girona, Spain

ARTICLE INFO

ABSTRACT

This paper presents the development of a robust automatic diagnosis technique that uses raw Electro-Mechanical Impedance (EMI) signals and deep autoencoder models to detect damage in fiber-reinforced-polymers (FRP) strengthened reinforced concrete (RC) elements, for which the most common failure modes occur in a sudden and brittle way by debonding. The contribution of this work is threefold: First, for the first time, two autoencoder models, convolutional and fully connected, based on an unsupervised learning framework supplemented by appropriate pre-processing techniques, are proposed for effective tracking of FRP-strengthened RC elements from raw EMI response variations in different locations of the auscultated structure; their implementation is also extensively investigated. The proposed framework consists of two main components, namely, dimensionality reduction and relationship learning. The first component is to reduce the dimensionality of the raw EMI signal while preserving the necessary information required, and the second component is to perform the relationship learning between the features with the reduced dimensionality and the stiffness reduction parameters of the structure. The approach is beneficial as only the EMI spectrum from the healthy structure state is considered for the training of the autoencoders. Second, the superior performance of the proposed framework is demonstrated. The results show that the proposed technique can accurately detect minor damage in its earliest stages for this kind of strengthened structures, while removing the need for manual or signal processing-based damage sensitive feature extraction from EMI signals for damage diagnosis. Finally, research presented in this work can potentially open up new opportunities for successful condition monitoring of this type of strengthened structures.

1. Introduction

Fiber Reinforced Polymers (FRPs) have been used in civil structures due to the advantages provided, including high tensile strength, light weight, the ability to customize the FRP properties, and good long-term durability [1–3]. Their application in reinforced concrete (RC) structures has been mostly for strengthening and rehabilitation of existing structures, by means of the external bonding of FRP sheets/strips [4–6] and Near Surface Mounted (NSM) [7–10]. With its increasing use and technological advances, the cost drawback for FRP becomes less acute, aided by an overall push requiring long-term performance, resiliency, and life-cycle cost considerations.

Debonding is the most common failure mode that could significantly affect the capacity of FRP strengthened RC members [11,12]. The

earliest stages of debonding, originated in a local way, if not detected, might lead to the sudden failure of the structure. Therefore, this type of structures should be inspected periodically to control potential damages which might cause its future failure. Several non-destructive testing (NDT) techniques might be used for surveillance in FRP composite- RC structures [13,14]. However, some of these tools are expensive and sometimes difficult to install the measurement equipment in the field. The electromechanical impedance/admittance (EMI/EMA) technique employing low-cost and small Piezo-electric ceramic lead Zirconate Titanate (PZT) transducers glued onto the structure plays an important role within the NDTs for SHM applications. EMI method has been applied for various structures [15,16] and under various load-induced stress [17], and its simple implementation, real-time capabilities and superior sensitivity to structural local damages make it very suitable to

---

* Corresponding author.
E-mail address: ricardo.perera@upm.es (R. Perera).

identify local damage in FRP strengthened RC structures like some applications in the past have demonstrated [18–22]. Local damage or material degradation can be identified by comparing EMI signatures acquired from a host structure at pristine and post-damaged states using some statistical indices. It could be obtained from previous works that EMI method has sufficiently demonstrated its effectiveness and reliability for monitoring damage in this type of structures, and, additionally, has a great potential to be developed into an autonomous and intelligent monitoring system able to automatically identify and characterize the correlation of damage with the dynamic variation of EMI spectra. The approach should avoid any extraction of hand-crafted characteristics of signals and subjective assessment, which might result in a wrong interpretation or loss of substantial information.

Deep learning (DL) techniques are a subset of machine learning (ML) and are regarded as a powerful tool to solve complex issue of damage classification by learning the representations of massive monitored data [23–25]. Among these, supervised convolutional neural networks (CNN) have recently emerged and proved to be successful in dealing with classification problems of large samples in domains such as computer vision, automatic video recognition, biomedical systems and recommender systems [26–28]. In the same way, CNN-based algorithms have also experienced a rapid advancement in relation to SHM in engineering [29–33]. These applications have demonstrated a high efficiency of CNNs in dealing with classification problems of large samples. DL approaches might also contribute to the implementation of intelligent monitoring based on EMI method and a few studies have also addressed the EMI-based damage quantification issues using CNN approach [34–36]. All these previous works show that the integration of the EMI with DL is feasible and promising.

However, strong limitations exist in CNN method about collecting sufficient reliable EMI samples. Large datasets representative of both the undamaged structure and the structure in different damage conditions are required to train efficiently a supervised learning network. Real-life structures cannot be artificially deteriorated to generate damaged data, therefore only data from the pristine structure are accessible, and unsupervised learning techniques are required. Consequently, over recent years, many studies have focused on approaches of unsupervised learning for the damage assessment in structures. Unsupervised learning is a process of learning from unlabelled data, such as datasets with undefined outputs that meet a general rule and may be grouped in a predictable pattern. Autoencoders are a popular and powerful deep learning technique that is widely used in anomalies detection. They are able to learn complex representations of the data, which allows them to detect anomalies that are not captured by traditional statistical methods. Due to their strong capacity for generalization, the application of autoencoders in vibration-based SHM has increased over the last few years [37–39]. Raw acceleration time series are used as the inputs for the autoencoder avoiding, in this way, the loss of information and exploiting the full potential of the neural network. Autoencoders models for anomaly detection are trained by learning the normal behavior of the structure (patterns of signals corresponding to intact conditions); no manual labeling of the training data is required. After that, the damage detection is implemented by checking whether the experimental data are fitted with the trained model or not.

This paper proposes the implementation of a convolutional autoencoder and a fully connected autoencoder for evaluating the damage condition of FRP strengthened RC elements from EMI signals. The autoencoder models encode the input raw impedance spectrum signals into low-dimensional representation and then the signals are reconstructed back at the decoder output. These networks offer the advantage of providing damage assessment without requiring additional damage labels, being highly sensitive to even minor damage occurrences. Damaged states of the structure are identified through the reconstruction capability of the autoencoders for different damage states. The main contribution of this study, to the knowledge of the authors, is that this paper makes the first attempt to combine autoencoders models and EMI techniques for monitoring of FRP-strengthened RC elements. A framework, which might be named as EMI integrated autoencoder, is developed to accurately predict the damage in FRP strengthened RC elements from raw EMI data without any pre-processing, which appears to be more accurate than using other metrics whose validity depends on several circumstances. The effectiveness of the proposed method is analyzed and quantified through a series of experiments. The method enables automatic data acquisition and identification of raw EMI signals, contributing to the real-time and intelligent monitoring and accurate assessment of the damage through the mechanical impedance change.

2. Electromechanical impedance method

The focus of this research is put on the development of the EMI-based damage assessment technique assuming that only reference or baseline data are labeled. EMI based techniques have shown a great potential in damage assessment and have been proposed in this work for structural health monitoring of FRP strengthened RC beams due to their high sensitivity to low levels of damage.

In EMI method, a PZT transducer is bonded to the surface of the monitored structure by using a high strength epoxy adhesive. Then, the transducer is electrically excited via an impedance analyzer. Due to electromechanical coupling of piezoelectric transducer and the host structure, mechanical resonances of the structure can be observed by measuring the electrical parameters of the piezoelectric transducer. With this method, Frequency Response Function of the impedance is evaluated with the use of one PZT transducer acting simultaneously as an actuator and a sensor.

To simplify its configuration, the patch can be regarded as a thin bar undergoing a uniaxial vibration along its length (x- direction) when an alternating electric field is applied in its thickness (z-direction). The host structure, connected on one side of the patch, is also assumed as a single-degree-of-freedom system, represented by its mechanical impedance. The coupled 1D electromechanical relationship was first introduced in [40] through the electrical admittance (reciprocal of the impedance), Y, of the PZT transducer as:

$$Y = G(\omega) + jB(\omega) = j\omega \frac{bl}{h}\left(\overline{\varepsilon}_{33}^{\sigma} - d_{31}^2 \overline{E}_{11}^E + \frac{Z_a(\omega)d_{31}^2 \overline{E}_{11}^E}{Z_a(\omega) + \xi Z_s(\omega)} \frac{\tan(\kappa l)}{\kappa l}\right) \quad (1)$$

where $G(\omega)$ and $B(\omega)$ are the conductance (real part of EMI) and susceptance (imaginary part of EMI), respectively; ω denotes the angular frequency of excitation; j is $\sqrt{-1}$; b, l and h are the width, length and thickness of the patch, respectively; and $\overline{\varepsilon}_{33}^{\sigma} = \varepsilon_{33}^{\sigma}(1 - \delta j)$ and $\overline{E}_{11}^E = E_{11}^E(1 - j)$ are the complex electric permittivity of the patch at a constant stress and the complex Young's modulus of the patch at a constant electric field, respectively; $Z_s(\omega)$ and $Z_a(\omega)$ are the mechanical impedance of the structure and the patch, respectively; κ is the wave number; δ is the dielectric loss factor of the patch; η is structural mechanical loss factor; d_{31} is the coupling piezoelectric constant.

Figure 1 shows a characteristic envelope spectrum of a strengthened concrete beam without and with damage, respectively.

Most of the work in the EMI technique depends on the change in the admittance signature of the structure between healthy and damaged states. More specifically, the conductance is more sensitive to mechanical damage of the host structure than the susceptance, which is more sensitive to the changes of environmental factors and sensor damage and its bonding [41]. Several metrics, such as root-mean square deviation (RMSD), mean absolute percentage deviation (MAPD), and correlation coefficient (CC), have been proposed to quantify this difference in the signature. However, as the admittance signatures have several troughs and peaks, the statistical metrics might become prone to be unstable in case of minor changes in the ambient conditions as well as measurement noise, predicting false damage identification. Furthermore, the sensitivity of alternative statistical indices is different depending on the
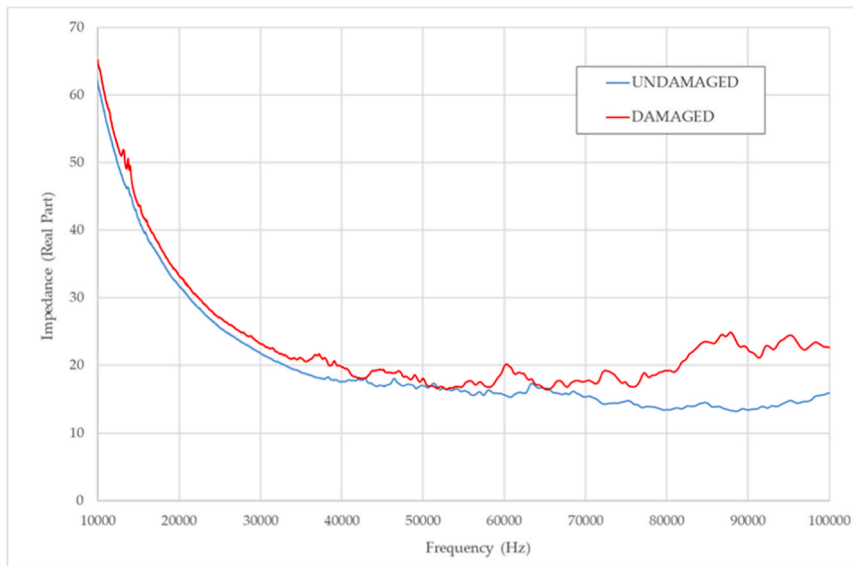
Fig. 1. Undamaged and damaged EMI spectrum of a FRP strengthened beam.

frequency band which reflects more clearly the damage to be identified. However, this frequency band cannot be determined in advance and its manual selection would involve not only a high cost but also a high probability of misjudgment if only a metric is used in the procedure. Given these shortcomings, exploiting directly the raw EMI signatures appears to be a more accurate alternative to detect damage and will be used in this work.

3. Methodology

In this section, the general scheme of the proposed damage identification algorithm and the procedure employed for EMI data acquisition and generation is detailed. Two different autoencoder neural network architectures have been used in the study. Considering the ability of autoencoders to learn features, their objective is to comprehend the dynamic characteristics associated with impedance signatures. Specifically, the two developed architectures are a convolutional autoencoder and an autoencoder with fully connected layers [42].

EMI data are characterized by high-dimensional nonlinearity and often contain irrelevant features or noise. These characteristics can lead to increased training complexity, overfitting, and other issues. Therefore, the use of effective feature dimensionality reduction methods to reduce the complexity and redundancy of the data is very important. Deep autoencoders are particularly effective to remove noise and those less important features. This makes them particularly useful in applications where data clarity and accuracy are crucial.

Furthermore, convolutional autoencoders add an additional benefit: they provide invariance to the spatial features of the data. This means they are sensitive to certain patterns in the data, regardless of their position in the function. In the context of EMI analysis for SHM, this allows convolutional autoencoders to identify patterns of damage or structural anomalies anywhere in the monitored structure, making them powerful and flexible tools for structural integrity analysis.

Next, both proposed autoencoders will be introduced as well as their training methodology.

3.1. Overview of proposed framework

The proposed method attempts to identify damage in FRP strengthened RC beams in an unsupervised way by using autoencoders. It means only EMI signatures in the intact beam state are needed for the training of each autoencoder models.

The proposed framework is illustrated in Fig. 2, which consists of three main components. The process begins with data acquisition. In our study, these data are gathered by subjecting a concrete beam to various loads. Upon applying each load, impedance measurements are taken using PZT sensors. These measurements are stored in a text file structured as a dataset.

Subsequently, data preprocessing is carried out. This step involves rearranging the data to make them suitable for neural network processing. Moreover, the data are normalized to optimize its handling and are divided into three sets: training data, validation data, and evaluation data. Training and validation data correspond to the undamaged or healthy beam which is assumed as baseline stage.

Once the data have been preprocessed, every autoencoder is trained using exclusively the training data. Subsequently to the training, the entire sequence of training data is fed again into the networks providing output data. A cost function defined by measuring the difference between the input and output data serves to define the deviation from the original model and, therefore, as novelty index or indicator of the structural damage. Finally, the detection performance of the whole algorithm can be evaluated on the testing dataset which contains both validation and evaluation data.
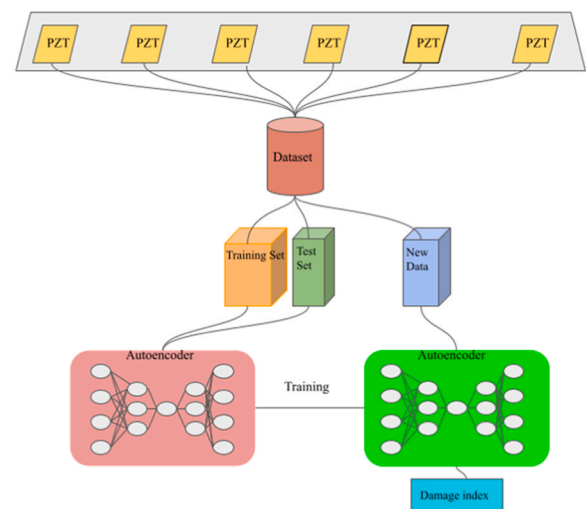

Fig. 2. General scheme of the algorithm used to quantify damage.

3.2. Data acquisition

The data set contains impedance responses captured with PZT transducers in different locations of the monitored structure and under different loading and damage conditions. All the impedances are measured for excitations between 10 and 100 kHz, with a frequency step of 12.5 Hz. It gives a total number of points in the Frequency Response Function of the impedance equal to 7201. The collected data are organized as a function of the loading stage, sensor number and frequency. Furthermore, for each combination of these parameters, both the real and imaginary values of the impedances, denoted respectively by $Z_r(\omega)$ and $Z_c(\omega)$, are recorded.

Most of free and open-source software libraries for machine learning and artificial intelligence support Python and JavaScript and mainly data in multi-dimensional structures or tensors. In this work, Tensor-Flow [43] and Pytorch [44] will be used. In machine learning the so called tensors play a big role since are fundamental data structures used to represent numerical data with multiple dimensions. Then, initially, the experimental data used in this study should be transformed to tensor format. In this context, a five-index tensor $\Psi_{\alpha\beta\mu\nu\gamma}$, whose indices refer to the sensor number, loading stage, frequency, real impedance, and imaginary impedance, respectively, is generated. Tensor indexing is a powerful technique that allows to select and manipulate specific elements or subsets of a tensor with ease. For instance, if α and β are selected to be one in the tensor, that means $\Psi_{11\mu\nu\gamma}$ will give the frequency and real and imaginary impedance values corresponding to the first sensor in the first loading stage.

3.3. Data generation and preprocessing

The raw EMI signatures containing the response of the structure for different loading stages and in different locations according to the location of the different PZT transducers are used as input data to the classification network. These measurements define the tensor $\Psi^{\alpha\beta\mu\nu\gamma}$ and carry information about the condition of the structure, including the possible existence of damage.

After obtaining the tensor $\Psi^{\alpha\beta\mu\nu\gamma}$, we proceed with its sorting and normalization, in order to prepare the data for network training.

Firstly, the non-essential information provided by the experimental tests is removed. As commented previously, the real part of the impedance is much more sensitive to mechanical damage of the host structure than the imaginary part. Hence, the tensor is decomposed as: $\Psi^{\alpha\beta\mu\nu\gamma} = \left\{ \Psi^{\alpha\beta\mu\nu}, \Psi^{\gamma} \right\}$, focusing solely on $\Psi^{\alpha\beta\mu\nu}$ henceforth.

Additionally, given that each sensor is processed individually since it provides only information of the structure in its vicinity, we segregate the tensor according to the first index, resulting in following form $\left\{ \Psi^{1\beta\mu\nu}, \Psi^{2\beta\mu\nu}, ..., \Psi^{9\beta\mu\nu} \right\}$. Then, for clarity, the notation is redefined so that the fixed index is at the bottom, $\Psi_\alpha^{\beta\mu\nu}$, i.e. three variables remain, the loading stage, the frequency points and the value of the real impedance in those points.

Subsequently, the impedance response of each sensor is individually standard normalized as each sensor data may have widely varying scales of response amplitude. Data normalization will contribute to accelerate the training and improve the generalization of neural networks. Min-max normalization is a very common method to normalize data and its purpose is to convert the impedance data in the frequency domain into a decimal between 0 and 1, according to the expression

$$\Phi_\alpha^{\beta\mu\nu} = \frac{\Psi_\alpha^{\beta\mu\nu} - Min(\Psi_\alpha^{\beta\mu\nu})}{Max(\Psi_\alpha^{\beta\mu\nu}) - Min(\Psi_\alpha^{\beta\mu\nu})} \tag{2}$$

where $\Phi^{\beta\mu\nu}$ is used to indicate the normalized impedance spectrum computed from the spectrum $\Psi_\alpha^{\beta\mu\nu}$.

As commented previously, only normal EMI signatures are used to train an unsupervised network. That means the tensors with which each network will be trained are $\Phi_\alpha^{1\mu\nu}$, i.e., only the undamaged initial loading stage will be used for this purpose.

One of the major drawbacks of the proposed framework lies in the considerable amount of EMI signals which are required to train the autoencoder models. To collect many EMI signals is unrealistic in practice since a lot of time should be consumed. Data augmentation is a widely-used technique to overcome this limitation. This technique allows to generate massive synthetic training data enhancing and increasing the diversity of training datasets, which will contribute to reduce overfitting issues of the network. In this work, to augment the number of impedance signatures, Gaussian noise perturbations were added into the normalized experimental EMI spectra. This method involves adding small random deviations generated from a Gaussian distribution to the original data, increasing the robustness and generalization capability of neural networks.

The probability density function of a Gaussian distribution is defined as

$$f(x|\mu, \sigma^2) = \frac{1}{\sqrt{2\pi\sigma^2}} e^{-\frac{(x-\mu)^2}{2\sigma^2}} \tag{3}$$

where μ represents the mean and σ^2 the variance. For the data augmentation process, the noise is centered around zero ($\mu = 0$). The standard deviation σ determines the magnitude of the perturbations. A small σ results in subtle perturbations, whereas a larger σ leads to more pronounced deviations.

To apply the Gaussian noise to the impedance functions, for each data point $Z(\omega_i)$, a random number $f(x_i)$ was generated from the Gaussian distribution. This process was repeated multiple times for each impedance function $Z(\omega)$, producing several augmented versions of the original data. In this work, each impedance spectrum $Z(\omega_i)$ was augmented 20 times by adding Gaussian noise. For each data point $Z(\omega_i)$, a random number $f(x_i)$ was generated from a Gaussian distribution with a mean of 0 and a standard deviation $\sigma = 0.01 \times Z(\omega_i)$. The value of $f(x_i)$ was truncated at 99.7 % to ensure that the random values do not exceed three standard deviations from the mean. The perturbed impedance function, $Z'(\omega_i)$, was then obtained using the equation:

$$Z'(\omega_i) = Z(\omega_i) + f(\omega_i) \tag{4}$$

It is essential to carefully select the appropriate σ value and assess the quality of the augmented dataset to ensure that the introduction of Gaussian noise enhances the neural network's training without introducing undesirable variability.

3.4. Autoencoders

3.4.1. Fully connected autoencoder

An autoencoder can be considered as an auto-associative neural network whose main aim is to learn a compressed representation of an input dataset, i.e. to convert an input vector into a code vector using a set of recognition weights, and subsequently, reconstruct the original or input data from this reduced representation using a set of generative weights.

A wide variety of autoencoder-based models have been used for representation learning and feature dimension reduction, handling large amounts of unlabeled recorded data. The simplest structure of a traditional autoencoder is the fully connected deep autoencoder (also known as dense). Its architecture (Fig. 3) consists of three main parts: an input layer, a hidden layer, and an output layer. The input and its corresponding output should be identical to each other. The hidden layer is formed by an encoder network, a decoder network, and a latent space. The encoder structure maps the input vector into a compressed hidden representation through successive layers with a decreasing number of neurons, which facilitates the reduction of dimensionality. The last layer of the encoder, with the smallest number of neurons, defines the latent space. This hidden layer or latent representation is the layer that
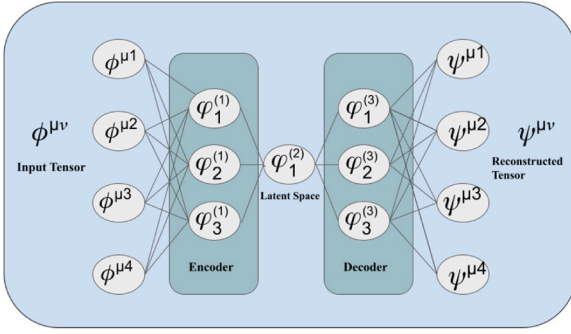
Fig. 3. General scheme of a deep autoencoder network.

contains a compressed and lower representation of input data. A bottleneck is imposed in the network to enforce a compressed knowledge representation in this hidden layer. Subsequently, the decoder maps the compressed hidden representation to a reconstruction of the original input by progressively increasing the number of neurons in each layer until reconstructing the original input as faithfully as possible.

Mathematically, from Eq. (2), an artificial neural network processes for each sensor, α, and each loading stage, β, the input tensor, $\Phi^{\mu\nu}$, through a series of encoder layers, reducing its dimensionality at each step:

$$
\begin{aligned}
h_{i\nu}^{(1)} &= \varphi^{(1)}\left(W_{i\mu}^{(1)}\phi^{\mu\nu} + b_i^{(1)}\right)\\
&\vdots \\
h_{w\nu}^{(N)} &= \varphi^{(N)}\left(W_{kw}^{(N)}h_{w\nu}^{(N-1)} + b_k^{(N)}\right)
\end{aligned}
\tag{5}
$$

where $h^{(i)}$ $(1 \leq i \leq N)$ is the encoded hidden representation, (W, b) represent the network's weights and biases, and $\varphi^{(i)}$ $(1 \leq i \leq N)$ are the activation functions for the encoder, which introduce non-linearities into the network. Due to the decreasing structure of the encoder, $w \leq j \leq i \leq \mu$.

After encoding, the network "decodes" the information, reconstructing the input tensor:

$$
\begin{aligned}
h_{\mu k}^{(N+1)} &= \varphi^{(N+1)}\left(W_{wk}^{(N+1)}h_{k\nu}^{(N)} + b_w^{(N+1)}\right)\\
&\vdots \\
\psi^{\mu\nu} &= \varphi^{(2N)}\left(W_{\mu i}^{(2N)}h_{i\nu}^{(2N-1)} + b_\mu^{(2N)}\right)
\end{aligned}
\tag{6}
$$

In this equation, $h^{(i)}$ $(N+1 \leq i \leq 2N)$ is the decoded hidden representation, and $\varphi^{(i)}$ $(N+1 \leq i \leq 2N)$ are the activation functions for the decoder, also nonlinear. The output tensor, $\psi^{\mu\nu}$, has the same dimensions as the input tensor.

The objective is to train the autoencoder to make the output as close to the input as possible. For it, a cost or loss function measuring the error between both must be minimized. Given the nature of autoencoders, this function is chosen as the root mean squared error (RMSE) between the input tensor and the reconstructed tensor:

$$
\epsilon = \frac{1}{2N}\sqrt{\sum_\mu \sum_\nu (\psi^{\mu\nu} - \phi^{\mu\nu})^2}
\tag{7}
$$

As the network is only trained with data captured from the intact beam, it will be only able to reconstruct raw impedances of the undamaged beam. The loss function is computed for the entire sequence of training data vectors providing a mean value which can be assumed as threshold to judge if damage occurs or not since, during the testing stage, sequences of impedance data (undamaged and damaged) are fed into the trained network. For each input data vector, the loss function is computed. If its value is higher than the defined threshold value it will be a symptom of damage.

3.4.2. Convolutional autoencoder

Convolutional neural networks (CNNs) are deep learning models used as high-performance estimators and classifiers specially to find patterns to analyze images. By applying a convolution operation on the input image through a convolution layer, a feature map of the image with its main patterns is created. This convolution layer is a unique layer that separates the CNNs from other neural networks and operates by applying a filter or kernel to the input data. A fundamental advantage of this kind of networks is their translational invariance what means a kernel can recognize a feature regardless of its location in the image. This is achieved by shifting the filter across the entire image.

Convolutional autoencoders are a variant of the CNNs structured in the typical form of an autoencoder, with an encoder block, a latent space, and a decoder block (Fig. 4). Unlike the fully connected autoencoders, in which dimensional reduction is achieved through dense layers, in convolutional autoencoders convolutional filters or kernels are used for this task.

An image is a two-dimensional plane composed of pixels. Then, when the convolution operation is applied, a function, K, moves over another function, I, calculating the sum of element wise multiplications as shown in the following equation

$$
(I * K)_{(x,y)} = \sum_{i=0}^{h-1}\sum_{j=0}^{w-1} I_{(x+i,y+j)} \bullet K_{(i,j)}
\tag{8}
$$

where h and w denote the height and width of the image, respectively.

In our problem, since raw EMI signatures are 1-D arrays in frequency domain, the convolutional layers process the data and learn to extract features, which are used for the classification task, in one dimension. In this case, the convolutional filters are vectors instead of matrices. The convolution operation is performed according to the following expression

$$
(I * K)[n] = \sum_{k=-\infty}^{\infty} I[n-k] \bullet K[n]
\tag{9}
$$

The convolutional autoencoder consists of repeatedly applying these convolution operations, reducing progressively the input dimensions to obtain a compact latent space.

The decoder process, on the other hand, seeks to increase the output dimensions using transposed convolution:

$$
y[n] = (x * h)[n] = \sum_{k=-\infty}^{\infty} x[k] \bullet h[n-k]
\tag{10}
$$

Although transposed convolution may seem like the inverse process of convolution, it is not its exact mathematical inverse. However, in the context of neural networks, it serves to reverse the dimension reduction effect of a convolution.

As with the traditional autoencoders, the main objective to be reached during the training is to minimize the difference between the input data and the output data. The same cost function of Eq. (7) can be
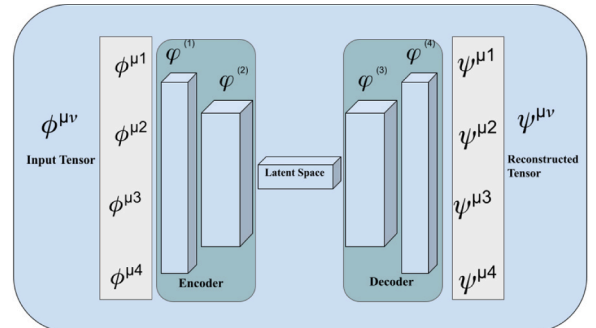

Fig. 4. General scheme of a deep convolutional autoencoder.

used for that purpose.

3.5. Autoencoder architecture

Both autoencoders, fully connected and convolutional, introduced in Sections 3.4.1 and 3.4.2, respectively, have been used in this work. The first one has been implemented on the PyTorch platform while for the second Keras platform was used. In our project, PyTorch was chosen for the development of the fully connected autoencoder, because of its intuitive interface and efficiency in debugging and prototyping, as well as its competent Autograd system for gradient calculation, making easier the experimentation with various autoencoder configurations. For the convolutional autoencoder, TensorFlow was used, given its outstanding ability to handle convolutional neural networks, its capability to scale efficiently, and the ease of implementing models on various platforms, essential qualities for practical applications that demand both flexibility and high performance. This decision represents the pursuit of a balance between agility in experimental development and efficiency in the practical application of the autoencoder models.

As commented previously, the architecture of the autoencoder network consists of the encoder and decoder (Figs. 3 and 4). In the encoder, the number of neurons in each layer will decrease. For the fully connected autoencoder, this transformation is carried out through a series of linear layers (Eq. (5)), immediately followed by activation functions of the PReLU type (Parametric Rectified Linear Activation). This type of activation function is a popular choice in deep learning and has the advantage of being computationally efficient and, additionally, can help prevent the vanishing gradient problem during training; it outputs the input value if it is positive, and outputs 0 if it is negative. Since the number of nodes decreases with each layer, the input vector is encoded into a low-dimensional vector. Specifically, the initial 7201-dimensional input is first condensed to 800 dimensions using a linear layer. Subsequently, a second linear layer carries out an additional reduction to 50 dimensions. Finally, the representation is compacted into an 8-dimensional latent space using a third linear layer.

On the other hand, the decoder operates inversely to the encoder. This means the resulting hidden representation from the encoder is then decoded back to the original space. This decoding process is carried out through alternating linear layers with PReLU activation functions. In its operation, the decoder initially expands the 8-dimensional latent space to 50 dimensions. Then, an additional expansion brings the representation to 800 dimensions. Finally, the representation is recovered to its original 7201 dimension.

Other configurations of the fully connected autoencoder model with more layers were also tested using a trial and error process but the loss function did not experience any improvement.

The detailed structure of the autoencoder network adopted in this work is outlined in the Table 1.

The convolutional autoencoder shares structural similarities with the traditional model, mainly in its division into encoder and decoder segments but, its distinctive feature lies in the incorporation of convolutional layers instead of linear ones.

The encoder segment is based on multiple Conv1D layers, specialized in executing one-dimensional convolutions. These layers, complemented with PReLU activation functions and L2 regularization, aim to identify local patterns and, consequently, reduce the dimensionality of the input data.

For its part, the decoder relies on Conv1DTranspose layers to reverse the compression process. These layers progressively expand the condensed representation until recovering the initial data dimensionality. Similar to the encoder, the layers integrated into the decoder also adopt PReLU activations and L2 regularization techniques to avoid overfitting.

As in the fully connected model, the configuration of the convolutional autoencoder involves a rigorous selection of a network architecture by means of a trial and error process with the goal of keeping the lowest reconstruction loss. At every trial selection of network architecture, the network was trained for 45 epochs with an input batch size of 5.

The performance of the network with configurations of 4, 5 and 6 encoding and decoding convolutional layers was studied. In the same way, different values (10^{-2}, 10^{-3}, 10^{-4}, 10^{-5}) of the L2 regularization parameter were checked.

The comprehensive structure of the convolutional autoencoder adopted in this study is shown in Table 2. The input layer is followed by five convolutional layers. In agreement with the reduction of the dimensionality of the data, the number of filters and kernel filter sizes decrease progressively from the first to the fifth convolutional layer. For the decoder module, the same number of convolutional blocks is used as in encoder but in the reverse direction. Finally, at the output layer. a linear activation function is used. Furthermore, the regularization was applied with a value of 10^{-3}.

3.6. Adam optimizer and model training

In this study, Adam optimization algorithm [45], an extension of the stochastic gradient descent algorithm, has been employed for the training of both autoencoders. Adam optimizer is characterized by adapting during the training the learning rates for each parameter or weight individually. To carry out this adaptation, the algorithm calculates an exponential moving average of the gradient and the squared gradient. For it, Adam defines two vectors, m and v, to accumulate the exponential moving averages of the gradient (first moment) and the squared gradient (second moment), respectively.

The weights, w, are updated after every iteration as follows:

$$w_{t+1} = w_t - \frac{\eta}{\sqrt{v_t} + \epsilon} m_t \tag{11}$$

where w_{t+1} and w_t are the weights at times $t + 1$ and t, respectively, η is the learning rate, m_t and v_t are the aggregates of gradient and squared gradient, respectively, at time t. Additionally, a stabilizing term, ϵ, is added to prevent divisions by zero.

The terms m_t and v_t are updated after every iteration using the

Table 1
Fully Connected Autoencoder Architecture.

Section	Layer Type	Input	Output
Encoder	Linear	7201	800
	PReLU	-	-
	Linear	800	50
	PReLU	-	-
	Linear	50	8
	PReLU	-	-
Decoder	Linear	8	50
	PReLU	-	-
	Linear	50	800
	PReLU	-	-
	Linear	800	7201
	PReLU	-	-

Table 2
Convolutional Autoencoder Architecture.

Section	Layer Type	Filters	Kernel	Activation
Encoder	Conv1D	64	5	PReLU
	Conv1D	64	3	PReLU
	Conv1D	32	3	PReLU
	Conv1D	16	3	PReLU
	Conv1D	8	3	PReLU
Decoder	Conv1DTranspose	8	3	PReLU
	Conv1DTranspose	16	5	PReLU
	Conv1DTranspose	32	5	PReLU
	Conv1DTranspose	64	5	PReLU
	Conv1DTranspose	64	10	PReLU
	Conv1D	-	3	Linear

following optimizers:

$$m_{t+1} = \beta_1 m_t + (1 - \beta_1)g_t \tag{12}$$

$$v_{t+1} = \beta_2 v_t + (1 - \beta_2)g_t^2 \tag{13}$$

where β_1 and β_2 are the parameters which control the decay rates of these moving averages, and g_t represents the gradient of the error with respect to the weights at time t.

Adam can be considered as a combination of two gradient descent methods, Momentum, and Root Mean Square Propagation. The choice of Adam as the optimizer of the autoencoders provides multiple benefits to the training process. Given its ability to adjust the learning rates individually for each coefficient, the algorithm tends to be less dependent on their initialization. Moreover, it offers greater robustness against disturbances and oscillations of the gradients, ensuring a more efficient and balanced training.

In our problem, the model is trained by randomly initialising the weights. The default configuration of the Adam optimizar ($\beta_1 = 0.9$, $\beta_2 = 0.999$, $\epsilon = 10^{-8}$, and learning rate $\eta = 0.0001$) was used for both autoencoders. The loss function defined in Eq. (7) was minimized with a batch size of 5 in 21 frames in each iteration and a no threshold in order to update the weights of the models. In summary, Table 3 shows the list of the hyperparameters used in the training of both autoencoder models.

4. Experimental validation and discussion

4.1. Experimental set-up

To validate the feasibility of the proposed approach, an experimental test campaign was conducted on a NSM-FRP strengthened reinforced concrete beam. A CFRP strip with a cross-section of 1.4 mm × 10 mm was used as NSM reinforcement in the tensile face of the beam specimen. The material properties of the concrete, the reinforcement steel and the CFRP were the following: a) Concrete: f_c = 30 MPa, E_c = 26 GPa, f_{ct} = 3 MPa; b) Steel: f_y = 500 MPa, E_s = 210 GPa; c) CFRP: f_{fu} = 2500 MPa, E_f = 170 GPa.

The total length of specimen was 1700 mm with a clear span between supports of 1500 mm and a concrete cross-section area of 120 mm wide and 175 mm height (Fig. 5). The top and bottom internal reinforcement consisted in two steel bars of diameter 6 mm. Steel stirrups of diameter 6 mm were used as shear reinforcement.

A series of monotonic static tests with the purpose of gradually introducing deterioration into the specimens were performed. The load was applied using a hydraulic jack through a steel beam with a span of 300 mm to distribute the symmetrical load. Concerning the loading procedure, from the baseline stage (D0) five loading steps (D1 to D5) were applied up to failure. The load level associated to each loading stage corresponds to the red circles of Fig. 6, which were identified from an analysis of the transformed section of the NSM-FRP strengthened RC concrete considering concrete cracking, steel yielding and FRP breakage.

Fig. 7 shows the experimental loading-unloading curves for each

loading step. The microstrain shown in this figure was captured with a FBG strain sensor bonded to the FRP bar and located where the left load point applies. In agreement with the predictions of Fig. 6, in the experimental tests, first cracks were detected during the second loading stage (D2). These cracks grew during the subsequent loading stages and, additionally, yielding initiated during the fourth loading stage (D4) as the reduction in slope in the load-strain curve demonstrates. In this stage, an important separation of concrete cover between two cracks occurred in the region located below the left load point (Fig. 8), which might have originated a premature secondary debonding close to this area. Finally, D5 is the stage immediately previous to the failure of the specimen, which occurred by FRP rupture. This secondary debonding phenomenon was localized as the slope of the curve in Fig. 7 increased.

Before the tests, the specimen was prepared for damage detection. For it, four PZT transducers (PZT1 to PZT4) were first glued externally on the FRP surface and other four (PZT6 to PZT9) were embedded into the structure by bonding them directly on the FRP strip using epoxy adhesive with high-shear modulus (Fig. 9). Two different sizes of sensors were used, P-876. A12 DuraAct (61 mm × 35 mm × 0.5 mm) for PZT1 and PZT2 and P-876. SP1 (16 mm × 13 mm × 0.5 mm) for sensors PZT3 to PZT9. Both types of sensors are formed of the piezoelectric material PIC255 whose properties are listed in Table 4.

With the purpose of measuring the change of the impedance across the different stages of the beam, the terminals of the PZTs were attached to an impedance analyzer (Agilent HP 4192 A) for acquiring the EMI signatures. To measure several transducers, the device was coupled with a 3499B multiplexor from Agilent as well. An excitation voltage of 1 V provided by the impedance analyzer was imposed on the PZT transducers. A scanning frequency from 10 to 100 kHz, with a step interval of 12.5 kHz (7201 sampling points) was selected for the tests. The electromechanical impedance was measured initially and after each loading step. The initial measurement under room temperature, defined as the impedance signal at the healthy state, served as a baseline for comparison. Five frequency sweeps were conducted for each sensor at each damage state, resulting in five impedance signals. Therefore, 30 measurements were taken by each PZT transducer.

The data arrays derived from the raw EMI signatures for the undamaged baseline stage were designated for training and validation of the autoencoders. Due to insufficient sample size and to avoid overfitting of the networks, until 100 additional impedance signatures were built for each loading stage by adding Gaussian noise perturbations into the normalized experimental EMI spectra. Fig. 10 illustrates an example of the non-noisy and noisy baseline impedance spectrum for sensor 3. Fig. 10a shows values for all the frequency range (10–100 kHz) while Fig. 10b is focused only on range 40–50 kHz.

EMI signatures in each damage condition and in each sensor were used to classify the stage of the beam in terms of damage severity and location.

4.2. Discussion

In this section, the capacity for damage detection of the two proposed autoencoders is evaluated using the scenarios presented in Section 4.1. For it, both models are trained using the impedance responses corresponding to a beam in healthy conditions (Scenario 0 in Section 4.1), i. e., the autoencoders are designed to accurately reproduce the signals of an undamaged beam, showing deficiencies when faced with a damaged beam signal. For training, 75 % of the baseline dataset was used, being the remaining 25 % used for validation.

To demonstrate how the trained model can be used for damage detection, the datasets associated to scenarios 1 to 5 in Fig. 6, which correspond to different damage severities, are used. Fig. 11 compares the measured (original) and reconstructed impedance spectra with both autoencoders for sensor 1 and for the six loading stages. The orange lines represent the model predictions, while the blue ones denote the experimental impedance signatures. The top panel displays the predictions of

Table 3
Hyperparameters used in the training of both autoencoder models.

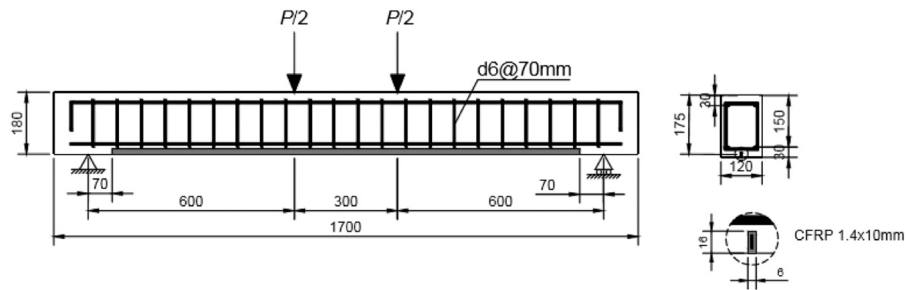| Hyperparameter	Value
Initial Weight Setting	Randomly Initialized
Optimizer	Adam
β_1	0.9
β_2	0.999
ϵ	10^{-8}
Learning Rate (η)	0.0001
Batch Size	5
Threshold	None
Loss Function	Defined in Eq. (7)
Epochs	Up to 45 (Early Stopping)

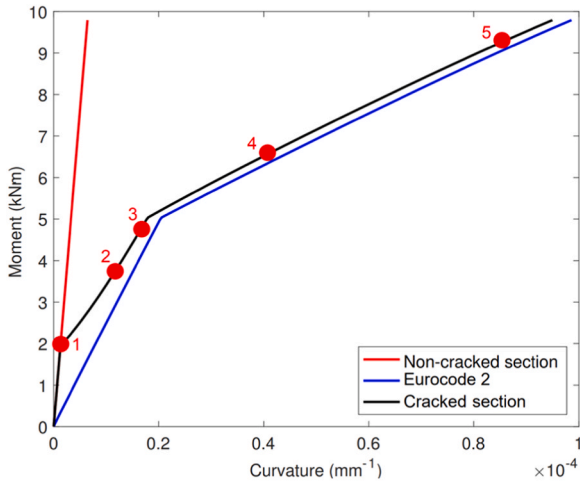**Fig. 5.** Geometry and loading scheme of the tested beam.

Fig. 6. Load-displacement curve for the tested beam.

since the discrepancy between the predicted and experimental signals shows a clear deviation. The peaks in the blue line are not suitably managed by the reconstructed signal. The reason for these inaccuracies is that damage produces modifications to the stiffness of the beam, which alter the impedance signatures. Since the proposed autoencoder models were trained using only the training dataset from the undamaged beam, it cannot generate accurate predictions regarding the unknown testing dataset from the damaged beam. This means that the reconstruction loss between the measured and reconstructed impedance spectra can be used as damage-sensitive feature.

Finally, load step 5 shows clearly a more pronounced divergence

Fig. 8. Cracks.

the convolutional autoencoder while the bottom panel those of the fully connected autoencoder.

Results for load step 0 show that both autoencoder models can accurately predict the undamaged impedance signature. For load steps 1 and 2, both models replicate also the impedance signals with considerable accuracy, which is a symptom of no damage or minor damage in the vicinity of sensor 1. However, for load steps 3 and 4, the proposed autoencoders predict the impedance spectrum with some inaccuracies

Fig. 7. Loading–unloading experimental curves.
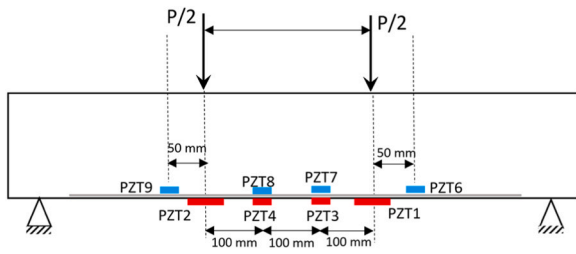
**Fig. 9.** Experimental set-up for the PZT sensors.

Table 4
Parameters of the piezoelectric material PIC255.

Property		Value
Density	ρ	7.80 g/cm³
Relative permittivity	$\varepsilon_{33}/\varepsilon_0$	1800
Relative permittivity	$\varepsilon_{11}/\varepsilon_0$	1750
Dielectric loss factor	$\tan\delta$	0.02
Piezoelectric strain coefficient	d_{31}	-180×10^{-12} C/N
Piezoelectric strain coefficient	d_{33}	400×10^{-12} C/N
Elastic compliance coefficient	S_{11}^E	16×10^{-12} m²/N
Elastic compliance coefficient	S_{33}^E	19×10^{-12} m²/N
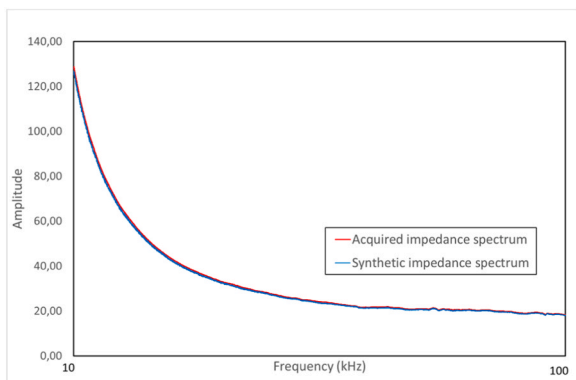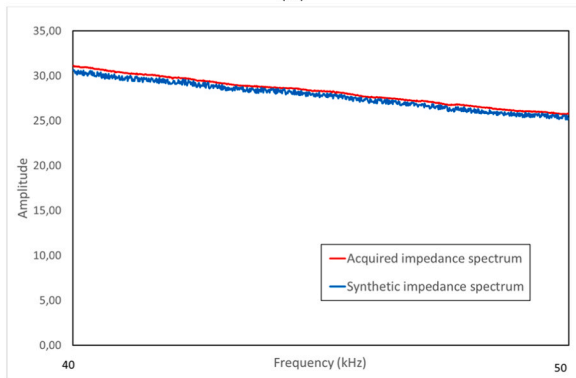
Fig. 10. An example of comparison between the non-noisy and noisy impedance baseline for PZT sensor 3: (a) All frequency range (10–100 kHz); (b) Frequency range (40–50 kHz).

associated to a very severe damage in the beam. It stands out that the convolutional autoencoder, unlike the fully connected one, produces a more coherent and uniform impedance prediction. Despite the higher coherence of the convolutional model, for the purposes of this research, the divergences observed in both models are fundamental, as they evidence significant differences between the prediction and the actual
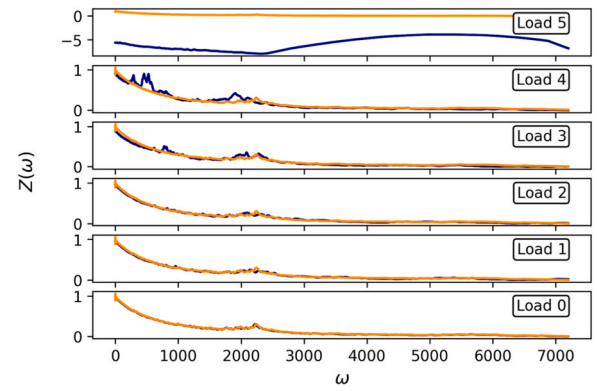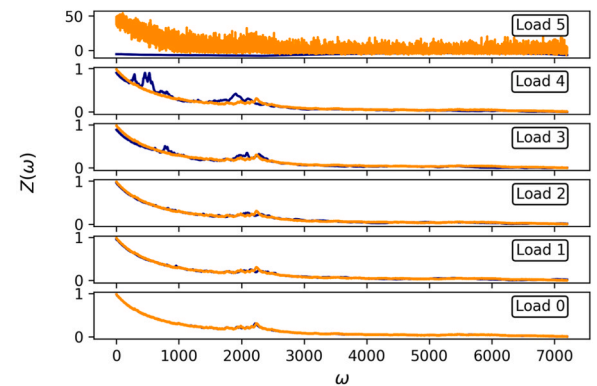

Fig. 11. Original and reconstructed impedance signals for PZT sensor 1: (a) Convolutional autoencoder; (b) Fully connected autoencoder.

measurement.

Since, as previously mentioned, both autoencoders allow extract automatically damage-sensitive features from the loss between the measured and reconstructed impedance spectra, Figs. 12 and 13 illustrate in the form of a histogram the RMSE distribution, computed with Eq. (7), of the proposed autoencoder models, corresponding to different beam damage scenarios and to the eight sensors. While each row in Fig. 12 corresponds to an external sensor (PZT1 to PZT4), the rows in Fig. 13 are referred to the internal sensors (PZT5 to PZT8). For both figures, plots on the left side were computed with the convolutional autoencoder while those on the right column were evaluated with the fully connected one. Both figures show clearly how the RMSE distribution of all damage scenarios (D0 to D6) varies from the undamaged case (scenario D0) as the level of damage increases. This variation of the RMSE distribution can be used in this study as damage indicator.

RMSE values show a tendency to increase as the applied load increases showing a clear distinction between the baseline stage and the rest of loading stages. In general terms, this tendency is common in all sensors, so it provides useful information to assess the structural integrity of the beam and shows the big potential of both autoencoder models for damage prediction. Additionally, it can be observed how the RMSE indices for stages 4 and 5 are significantly higher than for the rest of loading states for all sensors, and, therefore, all sensors report the same consistent information regarding the possible severity of changes at the last steps. This is especially significant in sensors 2 and 9, located in the same zone of the beam (Fig. 9), for which very high values of RMSE are reached indicating a severe damage in their vicinity.

Regarding both autoencoders, the performance is very similar for all sensors and loading stages, except for sensors 3 and 4, where a slight
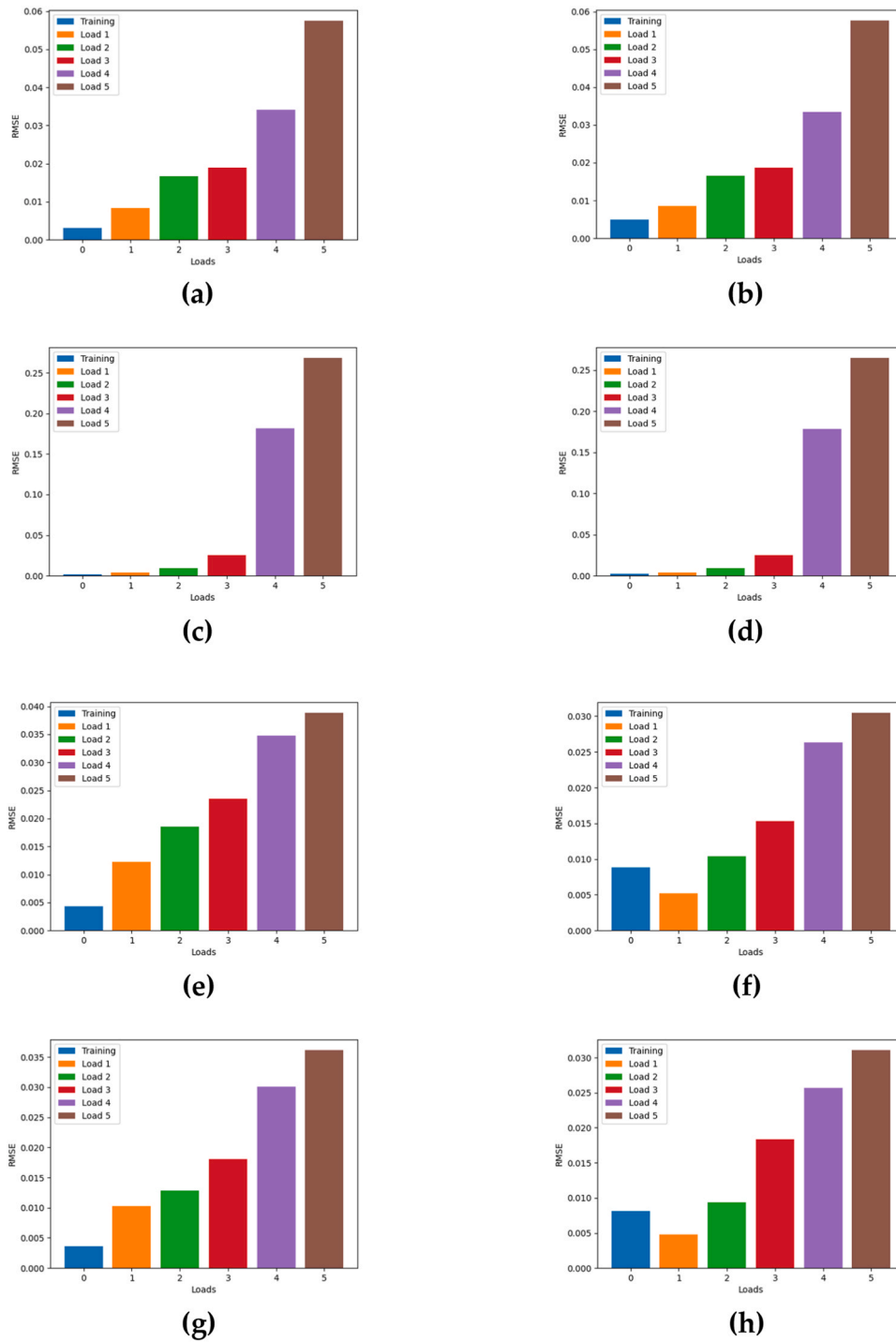
Fig. 12. RMSE distribution for PZT external sensors: (a) PZT1 - Convolutional AE; (b) PZT1 - Fully connected AE; (c) PZT2 - Convolutional AE; (d) PZT2 - Fully connected AE; (e) PZT3 - Convolutional AE; (f) PZT3 - Fully connected AE; (g) PZT4 - Convolutional AE; (h) PZT4 - Fully connected AE.

RMSE decrease between stages 0 and 1 occurs. This reduction might be due to small imprecisions in the estimation of the convolutional autoencoder, which are only evident for minor damage.

Complementarily, Fig. 13 demonstrates that the overall behavior of the internal sensors is consistent with the first four. However, a peculiarity is identified in sensor 8, where both networks detect a larger discrepancy already in load step 2. This observation suggests that the area corresponding to this sensor experiences such damage that discrepancies in subsequent load steps are comparable. In contrast, sensor 9 reiterates that damages in the early load stages are minimal. In summary, it can be inferred that the beam adequately withstands the first

three load steps, starting its fracture in the fourth step, and culminating in a break between the fourth and fifth steps.

Figs. 12 and 13 show that RMSE distribution grows significantly when the structure is damaged, making it an appropriate damage index. The variation of the RMSE distribution can be used, therefore, as damage indicator. In this sense, an index, DI_{LS}, based on the total distance between RMSE for any loading stage, $RMSE_{LS}$, and its value for the baseline stage, $RMSE_{Baseline}$, might be defined as follows

$$DI_{LS} = \frac{RMSE_{LS} - RMSE_{BASELINE}}{RMSE_{BASELINE}} \qquad (14)$$
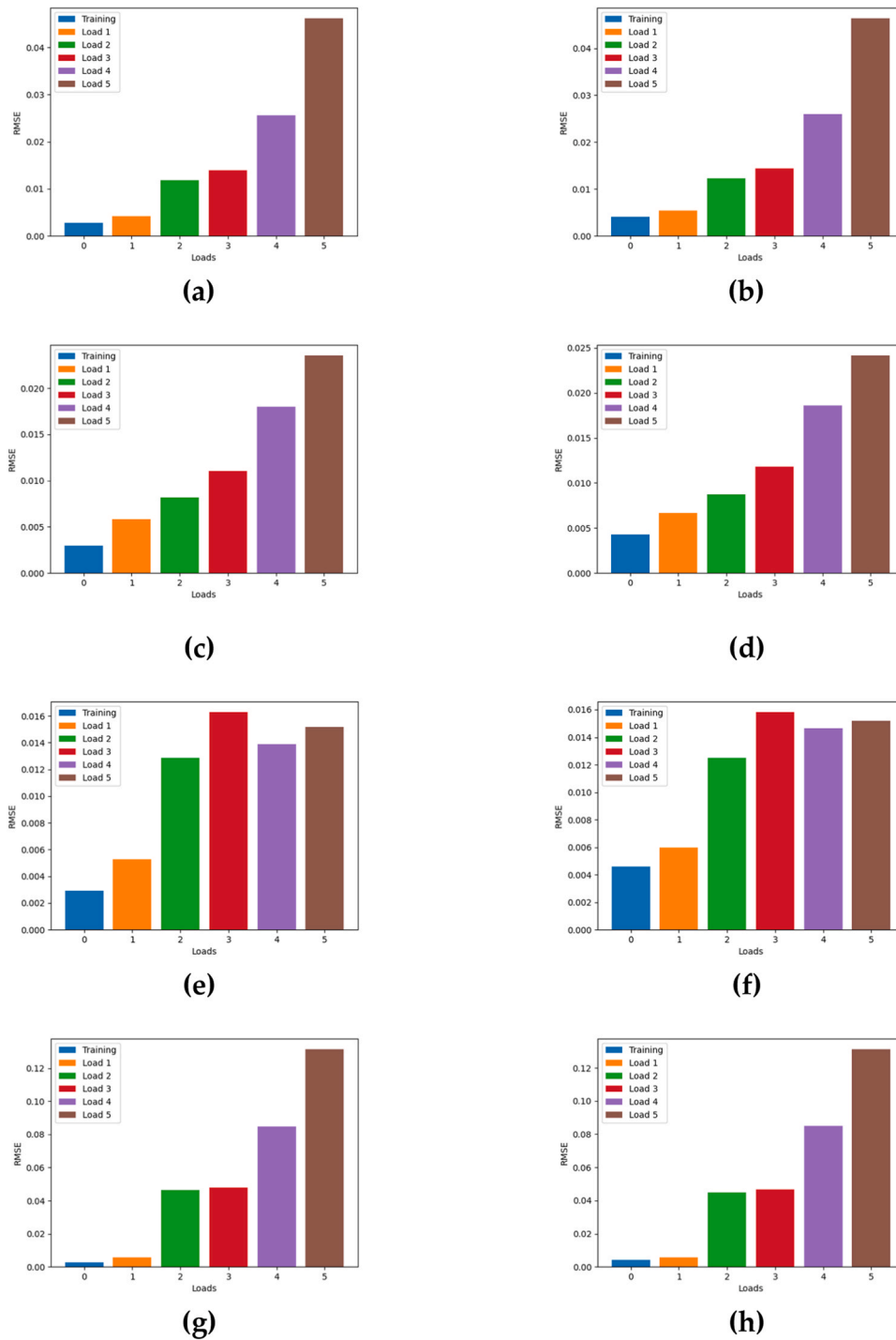
Fig. 13. RMSE distribution for PZT internal sensors: (a) PZT6 - Convolutional AE; (b) PZT6 - Fully connected AE; (c) PZT7 - Convolutional AE; (d) PZT7 - Fully connected AE; (e) PZT8 - Convolutional AE; (f) PZT8 - Fully connected AE; (g) PZT9 - Convolutional AE; (h) PZT9 - Fully connected AE.

This index should be evaluated for each sensor, assuming damage zero in case $RMSE_{LS} < RMSE_{Baseline}$. Fig. 14 shows the damage indices computed with Eq. (14) for all sensors and loading stages. In this figure, it is clear that the sensitivity of the damage index when convolutional autoencoder is used is higher that when fully connected model is applied. Furthermore, much higher damage indices are obtained for sensors PZT2 and PZT9 for loading stages 4 and 5, which agrees with the experimental observations. As commented in Section 4.1, before FRP rupture, a FRP premature secondary debonding originates during loading stages 4 and 5, in the region located where the left concentrated load applies. Sensors PZT2 and PZT9 are the closest sensors to this area

which would explain the extraordinary growth of the damage index experienced by both during fourth and fifth loading stages, in comparison with the remaining sensors, and the capacity of the proposed methodology to identify this debonding.
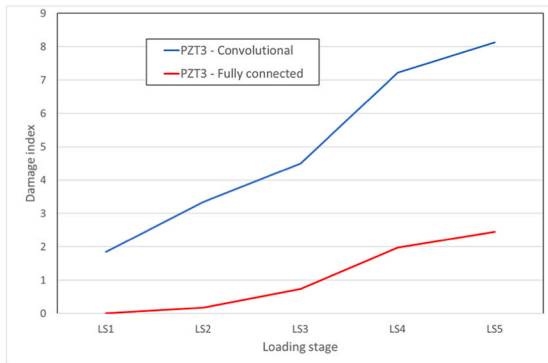
5. Conclusions

In this study, two deep autoencoder models, convolutional and fully connected, integrated with a statistical-pattern- recognition-based approach that uses raw EMI spectra captured from PZT transducers, have been proposed for structural damage assessment of FRP
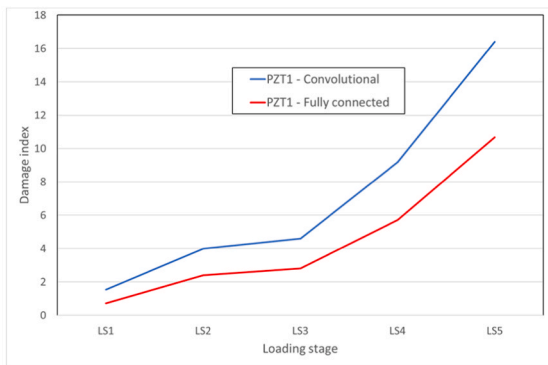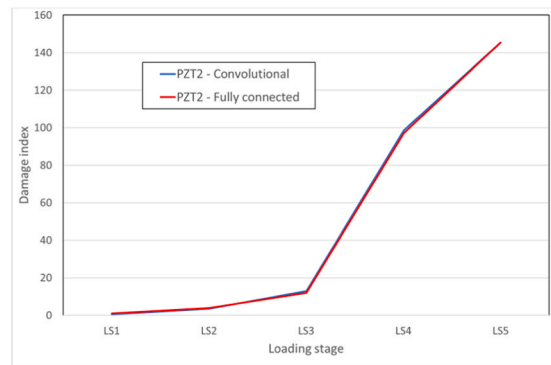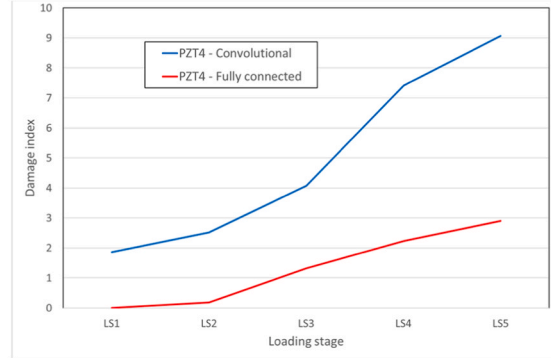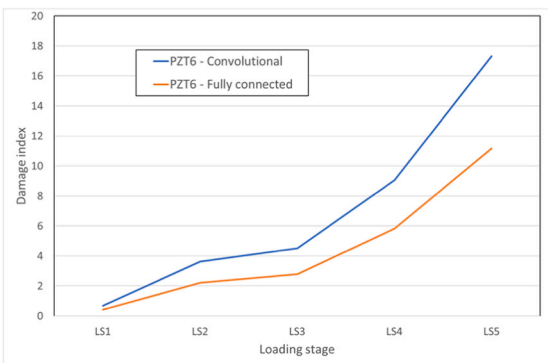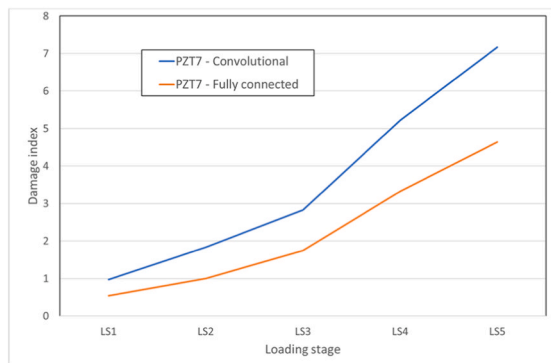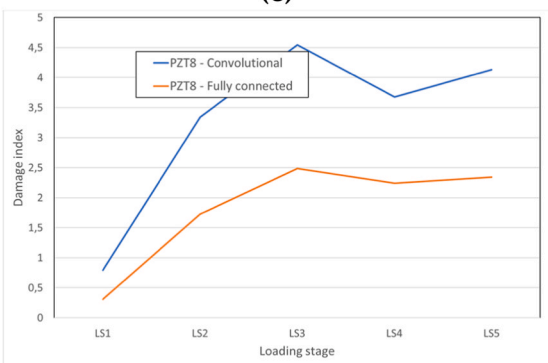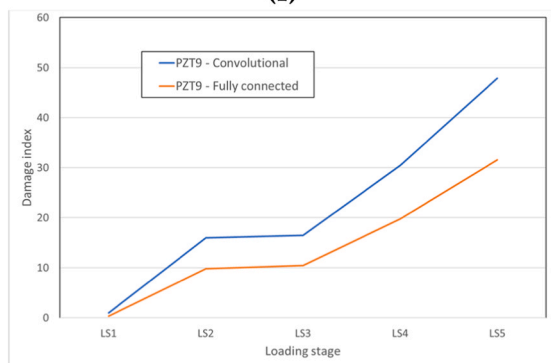
Fig. 14. Damage index: (a) PZT1; (b) PZT2; (c) PZT3; (d) PZT4; (e) PZT6; (f) PZT7; (g) PZT8; (h) PZT9.

strengthened RC elements. Exploiting directly the raw EMI signatures appears to be a more accurate alternative to detect damage than the use of other metrics derived from it which frequently drive to misjudgment.

The proposed method uses the raw EMI data obtained from the healthy structure to train the autoencoders since, unlike other deep learning methods, it does not rely on damage labels for training. The correctness of the two proposed approaches has been validated through several experimental tests, presented in Section 4.1, where has been shown that the error in signal reconstruction from the trained autoencoders is sensitive to damage, when considering EMI data from several stages of the tested beam. From this error, a damage index has been defined. Although the convolutional network has proved to be more consistent under certain damage stages, both approaches have effectively detected and identified the presence of minor damage in this type of strengthened structures as well as the secondary debonding previous to the failure, which provides valuable insights for their maintenance and safety assurance with the purpose of avoiding critical sudden and brittle failures for this type of strengthened structures.

For future work, a combined use of both autoencoder models in an ensemble procedure might provide a more detailed and accurate diagnosis of the structural health of the inspected structures, optimizing in this way the early detection of damage. Additionally, damage identification based on EMI under varying environmental conditions using autoencoders is also a challenge to be tackled in the future.

CRediT authorship contribution statement

Ricardo Perera: Writing – review & editing, Writing – original draft, Visualization, Validation, Supervision, Software, Resources, Project administration, Methodology, Investigation, Funding acquisition, Formal analysis, Conceptualization. **Marta Baena:** Visualization, Validation, Resources, Project administration, Methodology, Investigation, Funding acquisition, Formal analysis, Data curation. **Cristina Barris:** Visualization, Validation, Supervision, Resources, Project administration, Methodology, Investigation, Funding acquisition, Formal analysis. **Alejandra Gómez:** Validation, Software, Methodology, Investigation, Formal analysis. **Javier Montes:** Writing – original draft, Validation, Software, Methodology, Investigation, Formal analysis.

Declaration of Competing Interest

The authors declare that they have no known competing financial interests or personal relationships that could have appeared to influence the work reported in this paper.

Data Availability

Data will be made available on request.

Acknowledgements

References

[1] Bank LC. Composites for Construction: Structural Design with CFRP Materials. 1st ed.,. West Sussex: John Wiley and Sons; 2006.

[2] Balaguru P, Nanni A, Giancaspro J. CFRP composites for reinforced and prestressed concrete structures. A Guide to Fundamentals and Design for Repair and Retrofit. 1st ed.,. New York and London: Taylor and Francis; 2009.

[3] Kim TK, Park JS, Kim SH, Jung WT. Structural behavior evaluation of reinforced concrete using the fiber-reinforced polymer strengthening method. Polymers 2021; 13(5):780. https://doi.org/10.3390/polym13050780.

[4] Dong J, Wang Q, Guan Z. Structural behaviour of RC beams with external flexural and flexural–shear strengthening by FRP sheets. Compos Part B Eng 2013;44: 604–12. https://doi.org/10.1016/j.compositesb.2012.02.018.

[5] Perera R, Bueso-Inchausti D. A unified approach for the static and dynamic analyses of intermediate debonding in FRP-strengthened reinforced concrete beams. Compos Struct 2010;92(11):2728–37. https://doi.org/10.1016/j.compstruct.2010.04.006.

[6] ACI (American Concrete Institute). Guide for the design and construction of externally bonded FRP systems for strengthening concrete structures. ACI 440.2R-17. Farmington Hills, MI: ACI. 2017

[7] Zhang SS, Yu T, Chen GM. Reinforced concrete beams strengthened in flexure with near-surface mounted (NSM) CFRP strips: current status and research needs. Compos Part B Eng 2017;131:30–42. https://doi.org/10.1016/j.compositesb.2017.07.072.

[8] Dias SJE, Barros JAO, Janwaen W. Behavior of RC beams flexurally strengthened with NSM CFRP laminates. Compos Struct 2018;201:363–76. https://doi.org/10.1016/j.compstruct.2018.05.126.

[9] Al-Saadi NTK, Mohammed A, Al-Mahaidi R, Sanjayan J. A state-of-the-art review: Near-surface mounted FRP composites for reinforced concrete structures. Constr Build Mater 2019;209:748–69. https://doi.org/10.1016/j.conbuildmat.2019.03.121.

[10] Barris C, Sala P, Gómez J, Torres L. Flexural behaviour of FRP reinforced concrete beams strengthened with NSM CFRP strips. Compos Struct 2020;241:112059. https://doi.org/10.1016/j.compstruct.2020.112059.

[11] Al-Saawani MA, Al-Negheimish AI, El-Sayed AK, Alhozaimy AMA. Finite element modeling of debonding failures in FRP-strengthened concrete beams using cohesive zone model. Polymers 2022;14(9):1889. https://doi.org/10.3390/polym14091889.

[12] Ortiz J, Dolati SSK, Malla P, Nanni A, Mehrabi A. FRP-reinforced/strengthened concrete: state-of-the-art review on durability and mechanical effects. Materials 2023;16(5):1990. https://doi.org/10.3390/ma16051990.

[13] Dolati SSK, Malla P, Ortiz J, Mehrabi A, Nanni A. Identifying NDT methods for damage detection in concrete elements reinforced or strengthened with FRP. Eng Struct 2023;287:116155. https://doi.org/10.1016/j.engstruct.2023.116155.

[14] Ortiz J, Dolati SSK, Malla P, Mehrabi A, Nanni. Nondestructive testing (NDT) for damage detection in concrete elements with externally bonded fiber-reinforced polymer. Buildings 2023;14:246.

[15] Na WS, Baek J. A review of the piezoelectric electromechanical impedance based structural health monitoring technique for engineering structures. Sensors 2018; 18:1307.

[16] Cao P, Zhang S, Wang Z, Zhou K. Damage identification using piezoelectric electromechanical Impedance: a brief review from a numerical framework perspective. Structures 2023;50:1906–21.

[17] Naoum MC, Papadopoulos NA, Voutetaki ME, Chalioris CE. Structural health monitoring of fiber-reinforced concrete prisms with polyolefin macro-fibers using a piezoelectric materials network under various load-induced stress. Buildings 2023; 13:2465.

[18] Perera R, Pérez A, García-Diéguez M, Dopico-Valle JL. Active wireless system for structural health monitoring applications. Sensors 2017;17(12):2880.

[19] Sun R, Sevillano E, Perera R. Identification of intermediate debonding damage in FRP-strengthened RC beams based on a multi-objective updating approach and PZT sensors. Comp Part B 2017;109:248–58.

[20] Perera R, Torres L, Ruiz A, Barris C, Baena M. An EMI-based clustering for structural health monitoring of NSM FRP strengthening systems. Sensors 2019;19(17):3775.

[21] Perera R, Gil A, Torres L, Barris C. Diagnosis of NSM FRP reinforcement in concrete by using mixed-effects models and EMI approaches. *Comp Struc*t 2021;273:114322.

[22] Li D, Zhou J, Ou J. Damage, nondestructive evaluation and rehabilitation of FRP composite-RC structure: a review. Constr Build Mater 2021;271:121551.

[23] Zhou XQ, Huang BG, Wang XY, Xia Y. Deep learning-based rapid damage assessment of RC columns under blast loading. Eng Struct 2022;271:114949.

[24] Ghiasi A, Moghaddam MK, Ng CT, Sheikh AH, Shi JQ. Damage classification of in-service steel railway bridges using a novel vibration-based convolutional neural network. Eng Struct 2022;264:114474.

[25] Jiang T, Frøseth GT, Rønnquist A. A robust bridge rivet identification method using deep learning and computer visión. *Eng Struct* 2023;283:115809.

[26] Yang R, Singh SK, Tavakkoli M, Amiri T, Yang Y, Karami MA, et al. CNN-LSTM deep learning architecture for computer vision-based modal frequency detection. Mech Syst Signal Process 2020;144:106885.

[27] Sinha KP, Kumar P. Human activity recognition from UAV videos using a novel DMLC-CNN model. Image Vis Comput 2023;134:104674.

[28] Yan C, Razmjooy N. Optimal lung cancer detection based on CNN optimized and improved Snake optimization algorithm. Biomed Signal Process Control 2023;86:105319.

[29] Sony S, Dunphy K, Sadhu A, Capretz M. A systematic review of convolutional neural network-based structural condition assessment techniques. Eng Struct 2021;226:111347.

[30] Almutairi M, Nikitas N, Abdeljaber O, Avci O, Bocian M. A methodological approach towards evaluating structural damage severity using 1D CNNs. Structures 2021;34:4435–46.

[31] Yoon J, Lee J, Kim G, Ryu S, Park J. Deep neural network-based structural health monitoring technique for real-time crack detection and localization using strain gauge sensors. Sci Rep 2022;12:20204.

[32] Jia J, Li Y. Deep learning for structural health monitoring: data, algorithms, applications, challenges, and trends. Sensors 2023;23:8824.

[33] Sapidis GM, Kansizoglou I, Naoum MC, Papadopoulos NA, Chalioris CE. A deep learning approach for autonomous compression damage identification in fiber-reinforced concrete using piezoelectric lead zirconate titanate transducers. Sensors 2024;24:386.

[34] Li H, Ai D, Zhu H, Luo H. Integrated electromechanical impedance technique with convolutional neural network for concrete structural damage quantification under varied temperaturas. Mech Syst Signal Process 2021;152:107467.

[35] Ai D, Cheng J. A deep learning approach for electromechanical impedance based concrete structural damage quantification using two-dimensional convolutional neural network. Mech Syst Signal Process 2023;183:109634.

[36] Ai D, Mo F, Cheng J, Du L. Deep learning of electromechanical impedance for concrete structural damage identification using 1-D convolutional neural networks. Constr Build Mater 2023;385:131423.

[37] Ma X, Lin Y, Ma H. Structural damage identification based on unsupervised feature-extraction via variational Auto-encoder. Measurement 2020;160:107811.

[38] Zhang Y, Xie X, Li H, Zhou B. An unsupervised tunnel damage identification method based on convolutional variational auto-encoder and wavelet packet analysis. Sensors 2022;22(6):2412.

[39] Römgens N, Abbassi A, Jonscher C, Grießmann T, Rolfes R. On using autoencoders with non-standardized time series data for damage localization. Eng Struct 2024; 303:117570.

[40] Liang C, Sun FP, Rogers CA. Electro-mechanical impedance modeling of active material systems. J Intell Mater Syst Struct 1994;21(3):232–52.

[41] Gayakwad H, Thiyagarajan JS. Structural damage detection through EMI and wave propagation techniques using embedded PZT smart sensing units. Sensors 2022;22 (6):2296.

[42] Jana D, Patil J, Herkal S, Nagarajaiah S, Duenas-Osorio L. CNN and Convolutional Autoencoder (CAE) based real-time sensor fault detection, localization, and correction. Mech Syst Signal Process 2022;169:108723.

[43] TensorFlow. Available online: ⟨https://tensorflow.google.cn/⟩, 2019.

[44] Pytorch 2.0. Available online: ⟨https://pytorch.org/⟩, 2023.

[45] Reyad M, Sarhan AM, Arafa M. A modified Adam algorithm for deep neural network optimization. Neural Comput Appl 2023;35:17095–112.